communications earth & environment

Article

A Nature Portfolio journal

https://doi.org/10.1038/s43247-026-03489-w

Antarctic sea-ice loss shifts the Pacific Decadal Oscillation toward a positive phase

Check for updates

Hyein Jeong [1,2], Hyo-Seok Park [1,2] ✉, Sang-Wook Yeh [3], Eui-Seok Chung [4] & Shang-Ping Xie [5]

Antarctic sea-ice loss can influence climate far beyond the Southern Hemisphere, but its remote impacts and underlying mechanisms remain uncertain. Here we use numerical climate model experiments to show that reduced Antarctic sea ice triggers a response resembling the positive phase of the Pacific Decadal Oscillation. This pattern is characterized by sea-surface temperature cooling in the western North Pacific and warming in the eastern and subpolar Pacific. This transient adjustment unfolds over approximately 20 years. Mechanistically, the response is initiated by a strengthened interhemispheric thermal gradient that drives a southward shift of the Asian jet. Idealized experiments confirm that this jet shift generates low sea-level pressure anomalies over the western North Pacific, which intensify cold oceanic advection and reduce downward shortwave radiation. These findings imply that Antarctic sea-ice decline can act as a cross-hemispheric driver, potentially shifting the Pacific Decadal Oscillation toward a positive phase.

Antarctic sea ice has shown remarkable variability in recent decades, with modest expansion during the late 20th century followed by a rapid and unprecedented decline since 2016, especially in 2023–24 (refs. 1–5). This dramatic shift raises a pressing question of how Antarctic sea ice change influences the global climate system. While Arctic amplification has long been recognized as a driver of extratropical and tropical circulation changes, the role of Antarctic sea ice loss and associated Southern Ocean warming only began to be fully appreciated[6–12].

Recent modeling and diagnostic studies suggest that polar sea-ice retreat can account for a substantial fraction—on the order of one-third—of the global-mean temperature increase in long-term equilibrium, through surface-albedo and other radiative feedbacks[13–17]. These findings underscore the importance of sea-ice albedo feedbacks for Earth's energy balance, but their implications for climate evolution in the coming decades remain uncertain. To probe near-term impacts, several studies have tested the transient response to subpolar Southern Ocean cooling and warming by nudging regional Sea Surface Temperature (SST) in climate models[7,9,12]. These experiments revealed El Niño–like warming in the tropical eastern Pacific, maintained by cloud–radiative and wind–evaporation–SST feedbacks[18], and suggested that such a pattern can amplify the global climate response to Southern Ocean change.

Despite these advances, important uncertainties remain. Prior work has implicitly assumed that an El Niño–like mean-state change is the key pathway through which Southern Ocean excites global teleconnections[7,10,11,19]. Yet it is not clear whether this specific tropical adjustment emerges robustly across models and ensembles, nor how extratropical SSTs respond when the tropical mean state differs. In addition, most previous studies have conducted either idealized SST nudging or long-term equilibrium adjustment experiments over centuries[7,9,15,20], leaving the processes governing the transient and quasi-equilibrium responses to Antarctic sea ice loss less well understood.

A particularly important open question is whether Antarctic sea-ice loss can influence North Pacific climate variability, including the Pacific Decadal Oscillation (PDO). Although the PDO is often regarded as an internal mode, recent evidence indicates its sensitivity to external forcing, such as anthropogenic aerosol and greenhouse gas emissions[21]. This raises the possibility that Antarctic sea-ice decline itself could act as an external driver, reorganizing PDO-like variability.

Here, we address these gaps using five-member ensemble simulations from two coupled climate models—National Center for Atmospheric Research, Community Earth System model version 2 (NCAR CESM2; ref. 22) and Geophysical Fluid Dynamics Laboratory, Global Coupled Cli-

[1]Institute of Ocean and Atmospheric Science (IOAS), Hanyang University, Ansan, South Korea. [2]Department of Marine Science and Convergence Engineering, Hanyang University, Ansan, South Korea. [3]Department of Climate and Energy System Engineering, Ewha Womans University, Seoul, South Korea. [4]Division of Ocean and Atmosphere Sciences, Korea Polar Research Institute, Incheon, South Korea. [5]Scripps Institution of Oceanography, University of California San Diego, La Jolla, CA, USA. ✉e-mail: hspark1@gmail.com

mate Model version 2.1 (GFDL CM2.1; ref. 23)—in which Antarctic sea ice albedo is artificially reduced. This experimental design allows us to examine both the transient adjustment and the emerging quasi-equilibrium state, and to assess the robustness of remote SST responses across models with different sensitivities. By comparing ensembles, we highlight how Antarctic sea ice loss can shape North Pacific SST variability independently of concurrent tropical Pacific mean-state change, and we explore the dynamical pathways linking Southern Ocean warming to cross-hemispheric teleconnections.

Transient climate responses to Antarctic sea ice loss

The transient response to Antarctic sea ice loss captures the immediate adjustments of the climate system, which can exert remote impacts[8,24,25]. It also reveals the processes that establish SST cooling and warming patterns across ocean basins, which later evolve into equilibrium states. Figure 1 illustrates these transient climate responses in CESM2 and CM2.1. Reducing sea ice albedo substantially decreases the annual mean Antarctic sea ice concentration, though the magnitude of the loss varies (Fig. 1a, b). CESM2 exhibits relatively strong sea ice retreat for a given albedo reduction, whereas CM2.1 requires a larger forcing to produce a weaker response, reflecting its lower sensitivity to the sea ice–albedo feedback[26].

The loss of Antarctic sea ice is accompanied by surface warming in the Southern Ocean (Fig. 1c-f). This warming enhances air–sea heat fluxes and modifies regional circulation, with signals extending both toward the South Pacific Convergence Zone (SPCZ) and along the South American coast into the eastern tropical Pacific, a region highly sensitive to remote forcing from the Southern Ocean[11,12,25]. Such eastern tropical Pacific warming can amplify cloud–radiative feedbacks, linking Antarctic forcing to tropical climate variability[7,18], while broader Southern Ocean warming has been shown to exert strong influence on tropical rainfall and cross-hemispheric climate linkages[12].

Beyond the tropics, both CESM2 and CM2.1 produce a robust positive PDO-like anomaly structure across the North Pacific (Fig. 1c–f), but with distinct adjustment pathways. During the first decade (years 1–10; Fig. 1c, d), CM2.1 already exhibits strong cooling in the northwestern Pacific together with warming in the eastern and subpolar Pacific (Fig. 1d), while CESM2 shows only weak and patchy anomalies (Fig. 1c). By the second decade (years 11–20; Fig. 1e, f), the positive PDO-like pattern becomes much clearer in CESM2, with intensified cooling in the northwestern Pacific and warming in the eastern basin, particularly during boreal summer. The development timescale differs markedly between the two models: CESM2 requires nearly two decades for the positive PDO-like structure to emerge, whereas in CM2.1 it develops within just a few years (Fig. 1g, h). These contrasts indicate that while the positive PDO-like response is a robust cross-hemispheric feature, its timing and amplitude depend strongly on model physics and feedback strengths[27,28].

Atmospheric circulation and teleconnections induced by Antarctic sea ice loss

The positive PDO-like response is not uniform across seasons but is most pronounced during boreal summer (Supplementary Fig. 1). In particular, the northwestern Pacific cooling intensifies in June–August, as evident from the seasonal cycle of SST anomalies (Supplementary Fig. 1e, f). This seasonality implies that the positive PDO-like response in boreal summer is likely mediated by atmospheric circulation anomalies and teleconnection pathways that are more active during this season, thereby linking Antarctic sea-ice loss to extratropical Pacific variability.

To explore these mechanisms, Fig. 2 illustrates the associated atmospheric and oceanic adjustments in CESM2 and CM2.1. In both models, westerlies weaken to the north and strengthen to the south of their climatological core (Fig. 2a, b). This equatorward intensification is particularly evident over Japan and the western North Pacific (Supplementary Fig. 2). The southward shift of the Asian summer westerly jet is dynamically consistent with pronounced SST warming in the off-equatorial South Indian Ocean, where the warming steepens the meridional temperature gradient on the jet's equatorward flank through thermal-wind balance[29,30]. The southward displacement of the Asian jet modifies how the jet interacts with regional topography. As the jet moves southward and crosses the high terrain of the southern Tibetan Plateau, the large-scale flow must conserve potential vorticity, producing cyclonic anomalies downstream (e.g., refs. 31,32). This process helps explain why subtropical jet strengthening is consistently accompanied by negative sea-level pressure (SLP) anomalies and an associated cyclonic circulation over the western North Pacific (Fig. 2c, d). The two models differ in the latitude of maximum SLP depression: around 30–40°N in CM2.1, but farther poleward in CESM2.

The lower panels (Fig. 2e, f) show corresponding SST responses. Both models simulate substantial cooling in the western North Pacific, but the anomalies are stronger and displaced slightly southward in CM2.1 relative to CESM2. Figure 2g and h show ocean temperature advection in the surface mixed layer ($Q_{adv} = -\rho_0 C_p h(\boldsymbol{U}_m \cdot \nabla_h T_m)$). It appears that the development of cyclonic winds generates the southward advection of cold water from higher latitudes, contributing to the SST decrease between 40°N and 60°N, particularly in the Sea of Okhotsk. At lower latitudes (30°–45°N), increased cloud cover reduces incoming shortwave radiation by up to 5–6 W m^{-2}, further amplifying the surface cooling (Fig. 2i, j). The reduced incoming shortwave radiation is a primary factor for changing the net surface heat flux in the western North Pacific (Supplementary Fig. 3).

While the atmospheric response is strongest in summer, the oceanic footprint persists across seasons. Supplementary Fig. 4 shows that a PDO-like SST anomaly pattern remains evident during boreal winter (DJF), although the associated atmospheric circulation differs from that in summer. In winter, the response is characterized by an intensified Aleutian Low, rather than a jet-related anomaly. This low-pressure anomaly is associated with strengthened surface winds and anomalous ocean currents that promote cold-temperature advection from the western into the central North Pacific, together with warm advection in the northeastern Pacific. In CM2.1, the warm advection is particularly pronounced, reinforcing the substantial warming over the eastern subpolar gyre. These wintertime advective processes act to maintain and, in some regions, enhance the broad western-to-central North Pacific cooling that develops during summer (Supplementary Fig. 5), contributing to a robust basin-scale positive PDO-like signal throughout the year.

These results indicate that the emergence of low SLP and cyclonic winds associated with Antarctic sea-ice loss is a central mechanism behind the western North Pacific SST cooling, favoring a positive PDO-like pattern. A qualitatively opposite relationship has been noted in observations: during the period of moderate Antarctic sea-ice expansion from the 1980s to 2014, a persistent negative PDO-like pattern was present[33]. While the observed linkage likely reflects contributions from tropical variability and other forcings, the resemblance suggests that changes in Antarctic sea-ice extent may modulate PDO-like variability through hemispheric teleconnections. The unprecedented Antarctic sea-ice decline in 2023–24 (Supplementary Fig. 6), which coincided with the persistence of a negative PDO, highlights that an immediate phase reversal is unlikely; however, continued sea-ice loss could favor a transition toward a positive PDO within the coming decades, consistent with the ~20-year adjustment timescale in CESM2 (Fig. 1g). Our simulations further suggest that Antarctic sea-ice loss influences the extratropical Pacific primarily through a southward shift and strengthening of the Asian subtropical jet (Fig. 2a, b). This mechanism is consistent with recent study showing that biases in the North Pacific jet are central to PDO variability and its teleconnections[34].

Mechanisms linking Antarctic sea-ice loss to a southward shift of the Asian jet

To clarify the physical pathway linking Antarctic sea-ice loss to the Asian jet and North Pacific circulation response, Fig. 3 synthesizes ensemble-regression results from the CESM2 and CM2.1 experiments. Antarctic sea-ice loss induces hemispheric-scale surface warming that extends beyond the Southern Ocean into the Pacific, Indian, and Atlantic basins and the

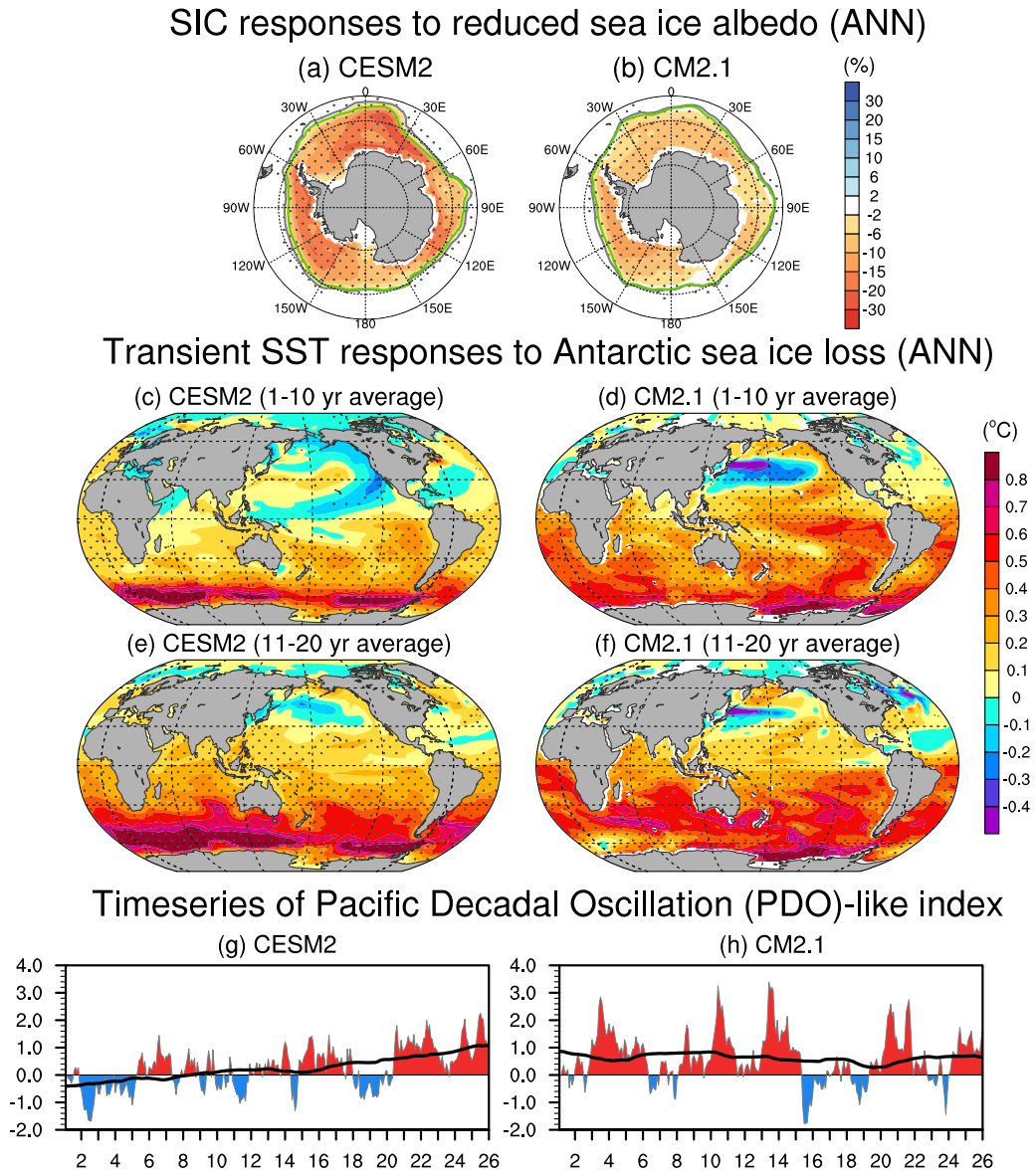


Fig. 1 | Transient climate responses to Antarctic sea ice loss in CESM2 and CM2.1. Sea ice concentration (SIC) anomalies (%) in annual mean (ANN) due to reduced Antarctic sea ice albedo for (**a**) CESM2 and (**b**) CM2.1, averaged over years 1-10 of the 100-year integration to represent the transient response. Gray and green lines denote the sea ice edges from the control and reduced Antarctic sea-ice albedo experiments, respectively. Annual mean sea surface temperature (SST; °C) anomalies for (**c, e**) CESM2 and (**d, f**) CM2.1, averaged over years 1–10 and 11–20, respectively. Stippling indicates regions where anomalies are statistically significant at the 95% confidence level. Timeseries of the Pacific Decadal Oscillation (PDO)-like index in **g** CESM2 and **h** CM2.1 during the first 26 years of integration. The PDO-like index is defined as the area-averaged SSTA over 50°–60°N, 180°–250°E minus that over 37°–45°N, 140°–180°E. The black line denotes the 10-year running mean.

tropics[12,18], producing a pronounced interhemispheric thermal asymmetry. We quantify this asymmetry using a cross-equatorial SST gradient over the Indo-Atlantic sector (ΔCross-SST), following previous studies showing that tropical Indian Ocean SST anomalies strongly influence the meridional displacement of the East Asian westerly jet[29,35–37]. More generally, inter-hemispheric Indo-Atlantic SST contrasts modulate cross-equatorial energy transport and the Hadley circulation, leading to coherent adjustments of the Asian summer circulation and jet latitude[38–40]. Recent work further identifies the Atlantic Ocean as an important remote driver of Asian westerly jet variability[41], supporting ΔCross-SST as a dynamically meaningful metric linking hemispheric thermal asymmetry to downstream circulation and SST responses over the western North Pacific.

The scatter relationships in Fig. 3a, b indicate that inter-ensemble variability in the Indo-Atlantic cross-equatorial SST gradient (ΔCross-SST) is strongly associated with both the southward displacement of the Asian subtropical jet (Fig. 3a; $r = 0.78$) and the intensity of negative SLP anomalies over the western North Pacific (Fig. 3b; $r = -0.70$). These relationships indicate that ΔCross-SST provides a compact representation of the strength of the remote atmospheric response across the two model ensembles.

The regression fields in Fig. 3c–f illustrate the intermediate dynamical pathway linking hemispheric thermal asymmetry to the Northern Hemisphere circulation response. When the Indo-Atlantic cross-equatorial SST gradient (ΔCross-SST) is stronger—corresponding to enhanced off-equatorial Southern Hemisphere warming—the zonal-mean overturning circulation exhibits an equatorward displacement of the Northern Hemisphere Hadley circulation together with an intensification of the cell (Fig. 3c). In this panel, contours denote the climatological zonal-mean meridional mass streamfunction, while the shading represents regression anomalies onto ΔCross-SST. The anomalous streamfunction displays a dipole structure across the Northern Hemisphere Hadley cell, with

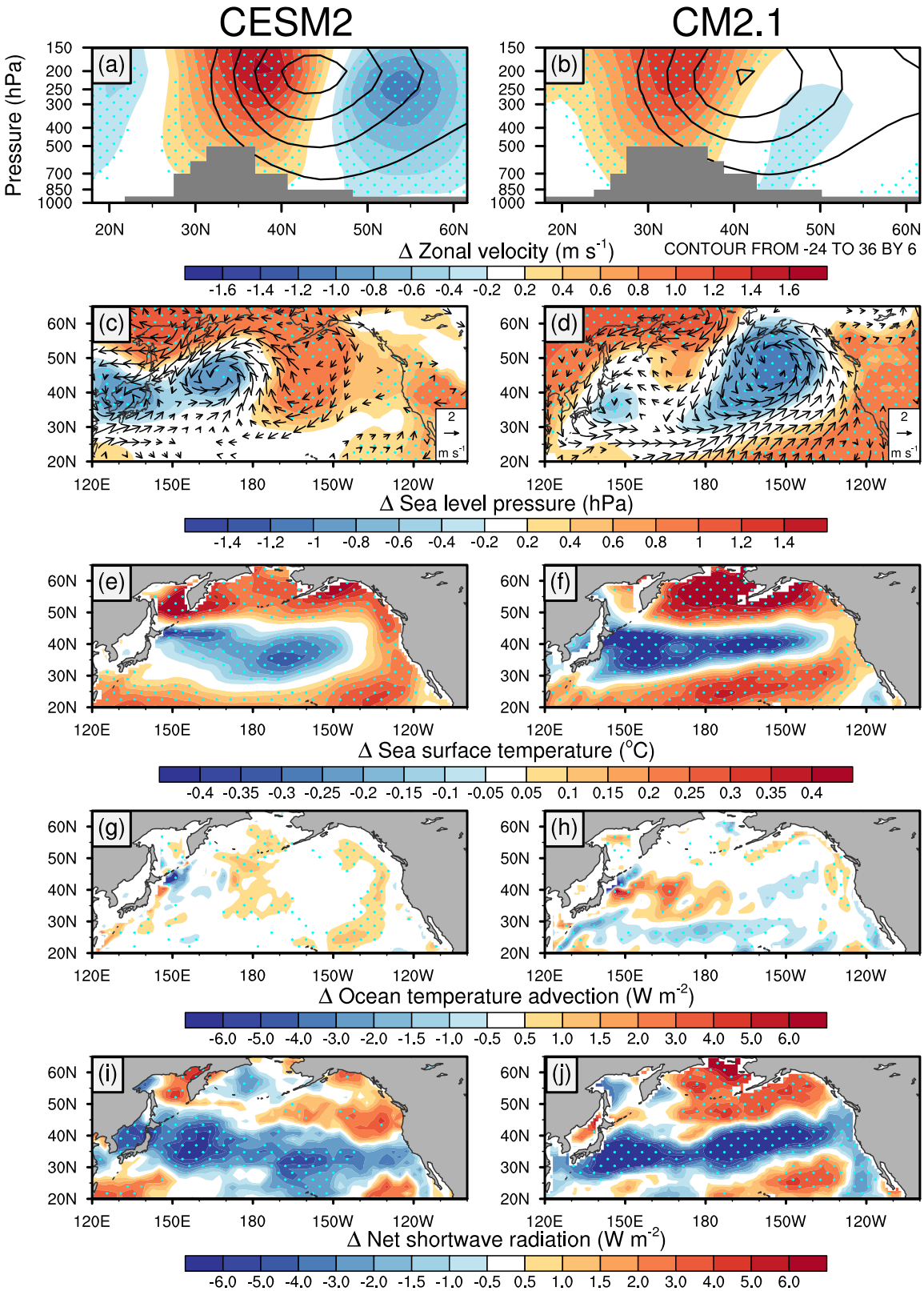


Fig. 2 | Atmospheric and oceanic responses to Antarctic sea ice loss during boreal summer (JJA) in CESM2 and CM2.1 models. Latitude–pressure cross-sections of zonal wind anomalies (m s^{-1}, shading) averaged over 80°E–180° in June–July–August (JJA) due to reduced Antarctic sea ice albedo for **a** CESM2 and **b** CM2.1, averaged over years 11–30 of the 100-year integration to represent the transient response. Contours show the climatological zonal wind (m s^{-1}). **c**, **d** Sea level pressure (hPa, shading) and surface wind anomalies (vectors), **e**, **f** SST anomalies (°C, shading), **g**, **h** ocean temperature advection anomalies in the mixed layer (ΔQ_{adv}; W m^{-2}), and **i**, **j** net surface shortwave radiation anomalies (ΔQ_{SW}; W m^{-2}). Statistically significant values ($p < 0.05$) are stippled.

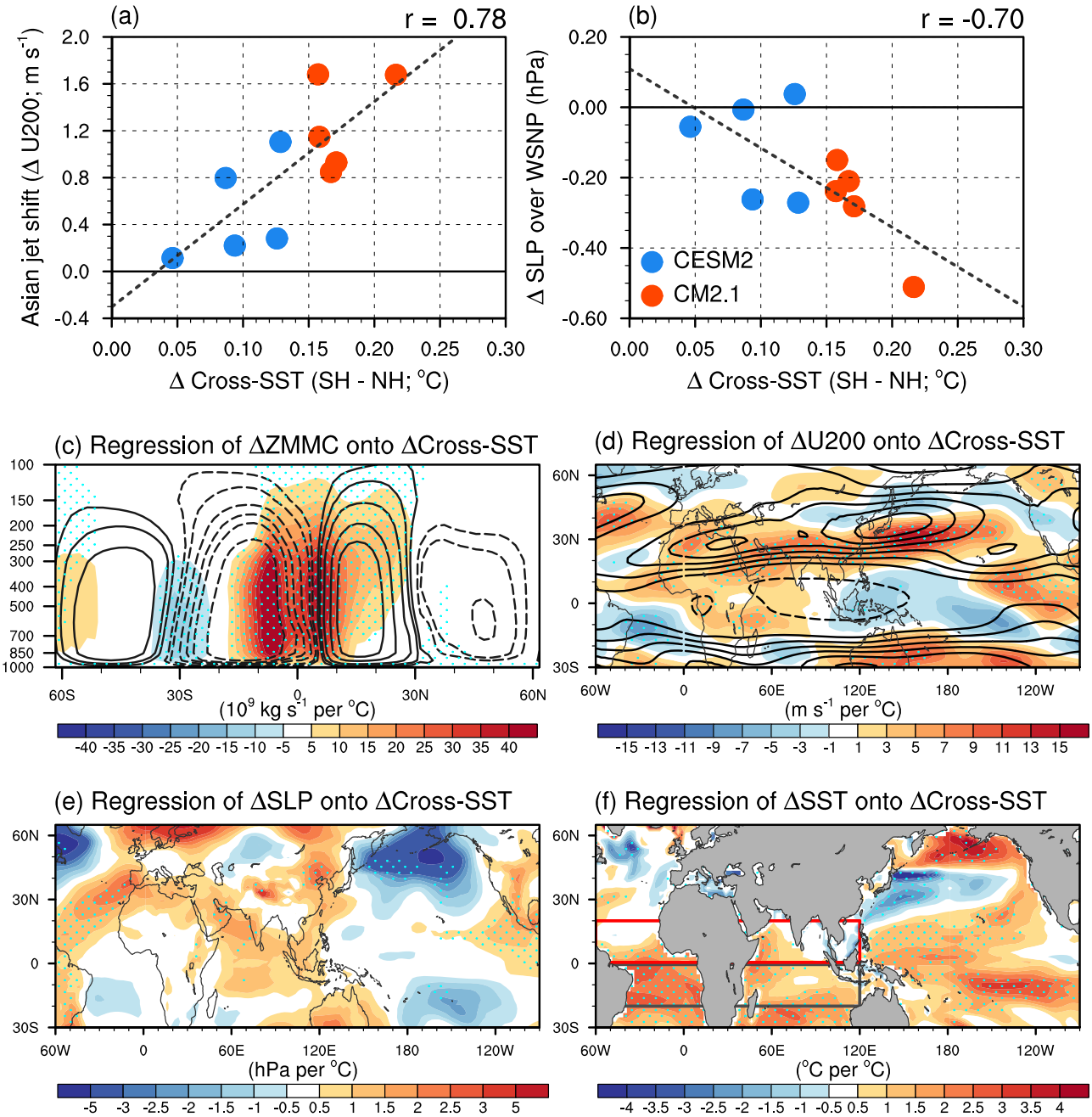


Fig. 3 | Dynamical pathway linking inter-hemispheric thermal asymmetry to the North Pacific circulation response. a, **b** Scatter plots showing the relationship between the inter-hemispheric SST gradient change (ΔCross-SST; defined as Southern Hemisphere minus Northern Hemisphere SST anomalies) and **a** the southward shift of the Asian westerly jet (ΔU200 index; m s^{-1}; 25°–35°N, 80°E–180°) and **b** the sea level pressure anomalies over the western North Pacific (ΔSLP index; hPa; 35°–50°N, 140°E–180°). Each dot represents an individual ensemble member from CESM2 (blue) and CM2.1 (red). **c**–**f** Regression maps of atmospheric and oceanic anomalies onto the ΔCross-SST index across ensemble members: **c** Zonal-mean meridional mass streamfunction anomalies (ΔZMMC; 10^9 kg s^{-1}), where shading represents regressed anomalies and contours show the climatological zonal-mean meridional mass streamfunction. **d** 200-hPa zonal wind anomalies (ΔU200; m s^{-1}), where shading represents regressed anomalies and contours show the climatological 200-hPa zonal winds. **e** Sea level pressure anomalies (ΔSLP; hPa), and **f** sea surface temperature anomalies (ΔSST; °C). In **f**, the red and gray boxes indicate the domains used to calculate the SST anomalies for the ΔCross-SST index (defined as the area-weighted SST difference between the Southern Hemisphere [20°S–0°, 60°W–120°E] and the Northern Hemisphere [0°–20°N, 60°W–120°E]). Stippling indicates statistical significance at the 95% confidence level.

enhanced overturning on its equatorward flank and weakened overturning on its poleward flank, indicating a latitudinal shift rather than a uniform strengthening. This adjustment reflects enhanced cross-equatorial energy transport required to balance the imposed hemispheric thermal contrast[42,43].

Consistent with this response, the upper-tropospheric westerlies exhibit an equatorward displacement and strengthening along the Asian jet exit region (Fig. 3d), in line with established Hadley–jet co-variability under hemispheric forcing[44,45]. The jet shift, in turn, favors the development of a cyclonic low-SLP anomaly over the North Pacific (Fig. 3e), which is linked to the western North Pacific SST cooling and eastern–subpolar warming pattern (Fig. 3f) that closely resembles a Positive PDO–like response, consistent with previous analyses

connecting North Pacific circulation anomalies to jet latitude shifts and air–sea interaction[46,47].

Previous studies utilizing the Indian Ocean Capacitor framework emphasized that basin-wide warming induces a subtropical anticyclone (High) over the western North Pacific[48,49]. In contrast, our regression onto the inter-hemispheric thermal gradient (ΔCross-SST) reveals a coherent southward shift of the Asian jet and a distinct mid-latitude cyclonic (Low) anomaly east of Japan. This suggests that the inter-hemispheric energy constraint overrides the local tropical wave response, favoring the mid-latitude cyclonic flow responsible for the observed cold advection and positive PDO-like pattern.

Idealized wind nudging experiment: impacts of the southward shift of the Asian jet

To validate this dynamical interpretation and assess causality, we next employ an idealized zonal-wind nudging experiment that isolates the impact of a southward displacement of the Asian jet on the North Pacific Ocean. Figure 4 shows the climate response to this experiment, in which the Asian westerly winds are nudged to reproduce the southward jet shift simulated in the Antarctic sea-ice loss experiments.

Here, the westerly wind nudging is confined to upstream of the western North Pacific, mostly in Central Asia, including the Tibetan Plateau, in order not to directly alter the heat and momentum balance in the western North Pacific. While the nudging is confined to upstream, it produces a southward shift of westerly winds, most evident in East Asia and western North Pacific, the exit region of Asian jet (Fig. 4a). The vertical cross-section averaged over Central–East Asia (40°–90°E) also exhibits a strengthening of an equatorward flank of westerlies, implying a strengthening of Asian subtropical jet (Fig. 4b). The structure closely resembles the jet displacement seen in the Antarctic sea ice loss experiments (Fig. 2a, b), though the amplitude of the anomalies is stronger in this idealized nudging experiment.

The jet shift is accompanied by broad negative SLP anomalies and a cyclonic circulation centered over the western North Pacific (Fig. 4c). This SLP pattern is generally consistent with those simulated in the Antarctic sea ice loss experiments (Fig. 2c, d), verifying that the development of low SLP in the western North Pacific is dynamically tied to the strengthening of Asian subtropical jet, i.e., equatorward shift of westerly winds over Asia. This SLP anomalies are accompanied by SST cooling in the western North Pacific (Fig. 4d). The cooling pattern resembles that in Fig. 2e, f, though the signal in the nudging experiment is more spatially confined to the western North Pacific, whereas the Antarctic sea ice loss experiments also show broader anomalies extending eastward.

Further analysis indicates that the SST cooling in the western North Pacific is mostly driven by reduced downward shortwave radiation (Fig. 4f), which explains the majority of net surface heat flux changes (Supplementary Fig. 7). Meanwhile, the role of ocean temperature advection is far smaller than those of the Antarctic sea ice loss simulations and is confined to the Sea of Okhotsk (Fig. 4e), possibly because the southward shift of the Asian jet modifies atmospheric circulation and cloud cover on relatively short timescales, leading to immediate changes in surface radiation, whereas oceanic advection typically operates on longer timescales.

Taken together, these comparisons indicate that the equatorward shift of the Asian westerly jet is one of key atmospheric pathways linking Antarctic sea ice loss to western North Pacific SST cooling and, ultimately, to the development of a positive PDO-like pattern. The zonal wind nudging experiment confirms causality by reproducing the circulation and SST anomalies seen in the sea ice loss simulations, while also clarifying that Antarctic forcing induces the response indirectly through its impact on the Asian jet.

The nudging experiment confirms the causal role of the Asian jet shift and helps to explain the distinct response timescales between CESM2 and CM2.1 (Fig. 1g, h). As shown in Supplementary Fig. 8, the initial atmospheric response in CESM2 (Years 1–5) is characterized by a weak northward displacement of the Asian westerly jet, accompanied by muted SLP and SST anomalies. This early response is consistent with a near-zero Indo-Atlantic cross-equatorial SST gradient during the same period (Supplementary Fig. 9). In CESM2, it takes approximately five years for the cross-equatorial SST gradient to become distinctly positive—with Southern Hemisphere SSTs cooling less than those in the Northern Hemisphere—after which the jet shifts equatorward and western North Pacific cooling intensifies. In contrast, CM2.1 exhibits a substantially larger cross-equatorial SST gradient that becomes positive within the first few years of forcing (reaching ~0.2 °C; Supplementary Fig. 9). This is consistent with the rapid equatorward jet shift and the fast emergence of the PDO-like response. These results indicate that the onset timing of the Asian jet response is sensitive to the magnitude and early development of the Indo-Atlantic cross-equatorial SST gradient.

Quasi-equilibrium SST responses to Antarctic sea ice loss

Figure 5 shows the quasi-equilibrium SST responses to Antarctic sea ice loss, averaged over years 71–100 of model simulations. The ensemble-mean patterns from CESM2 and CM2.1 both exhibit global ocean warming, but with notable differences in the tropical Pacific. CESM2 shows a relatively weak east–west contrast (Fig. 5a), while CM2.1 features stronger warming in the west relative to the east, producing a more La Niña–like structure (Fig. 5b). To illustrate the ensemble spread, we present selected members from each model. Some realizations, such as the second CESM2 and fourth CM2.1 runs, display El Niño–like warming in the eastern Pacific (Fig. 5c, d), consistent with earlier studies that emphasized this pathway (e.g., refs. 7,11,12,18,25). By contrast, other members, such as the fourth CESM2 and fifth CM2.1 runs, exhibit La Niña–like responses (Fig. 5e, f). The full five-member ensembles, shown in Supplementary Fig. 10, confirm this diversity.

The east–west SST contrast in the equatorial Pacific (Fig. 5g, h) highlights this spread: while some ensemble members exhibit strong El Niño–like or La Niña–like responses, the ensemble means are modest, with CESM2 leaning toward weak eastern Pacific warming. These results suggest that although the tropical Pacific equilibrium response to Antarctic sea-ice loss is generally El Niño–like[11,12,18,25], strong internal variability leads to diverse quasi-equilibrium responses across the ensembles and climate models.

Despite the ensemble-dependent tropical responses, both models consistently produce a positive PDO-like pattern in the North Pacific, including western North Pacific cooling or delayed warming (Fig. 5a–f). This outcome is partly consistent with the inverse relationship suggested by observations: during the late twentieth and early twenty-first centuries, when Antarctic sea-ice extent moderately expanded, a negative PDO trend was observed[33]. Our results in Figs. 2 and 4 point to the equatorward shift of the Asian westerly jet as a key driver of this cooling, through enhanced cold ocean advection and reduced downward shortwave radiation. However, we acknowledge that other mechanisms—such as changes in tropical–extratropical interactions[50–54], eddy feedbacks[55–57], or internal variability[58,59]—may also contribute to shaping the equilibrium SST pattern. Thus, while the Asian jet displacement provides a physically consistent explanation for the western North Pacific cooling, a full attribution of the positive PDO-like structure likely involves multiple processes (e.g., refs. 60,61).

Conclusions

Our experiments demonstrate that Antarctic sea ice loss exerts robust influences on remote oceans, extending its impact far into the Northern Hemisphere. In both CESM2 and GFDL-CM2.1, the imposed sea-ice decline triggers a basin-scale positive PDO-like response, expressed as western North Pacific cooling and eastern–subpolar Pacific warming. Figure 6 summarizes this dynamical chain and the distinct temporal pathways. While the Antarctic-induced southward shift of the Asian jet serves as a common atmospheric bridge, the response timing varies—immediate in CM2.1 (Years 1–5) but delayed in CESM2 (Years 6–20). Regardless of the pace, this jet displacement consistently generates cyclonic anomalies that

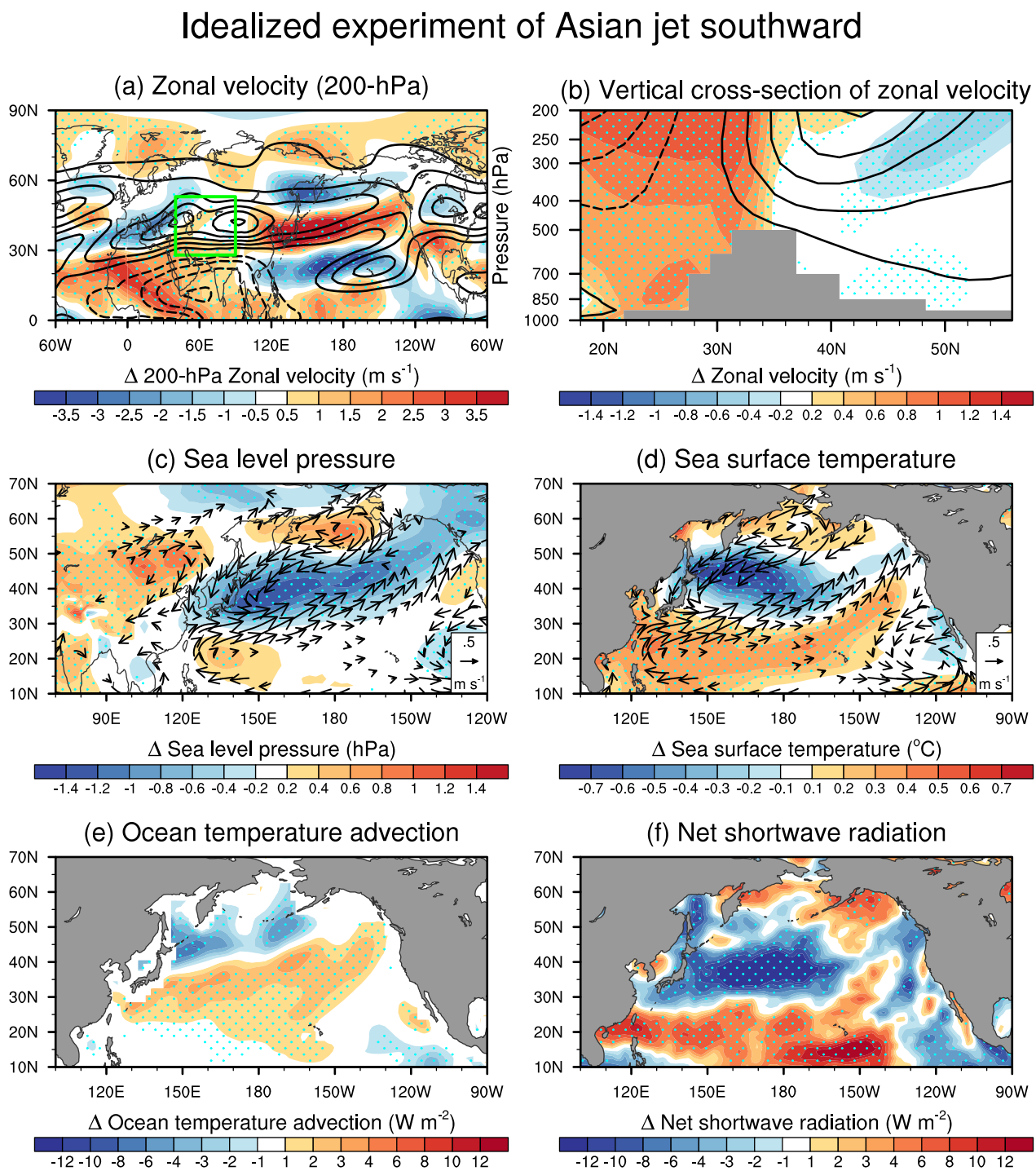


Fig. 4 | Climate response to an idealized southward shift of the Asian jet. a Zonal wind anomalies (m s^{-1}, shading) at 200 hPa in June–July–August (JJA) from the southward-shifted Asian jet nudging experiment. The green box marks the zonal wind nudging region (28°–53°N, 50°–100°E). **b** Vertical cross section of zonal wind anomalies (m s^{-1}, shading) averaged over 40°–90°E. Contours in (**a**, **b**) show climatological zonal wind (m s^{-1}) from the control simulation. **c** Sea level pressure (SLP; hPa, shading) and surface wind anomalies (vectors). **d** SST (°C, shading) and surface wind anomalies (vectors). **e** Ocean temperature advection anomalies (ΔQ_{adv}; W m^{-2}) in the mixed layer. **f** Net surface shortwave radiation anomalies (ΔQ_{SW}; W m^{-2}). Stippling indicates statistical significance at the 95% confidence level.

drive cold advection and reduced shortwave radiation, ultimately resulting in a positive PDO-like state. Idealized zonal-wind nudging experiments confirm that a southward displacement of the Asian westerly jet provides a central dynamical pathway for this response, by enhancing cold ocean advection from higher latitudes and reducing shortwave radiation over the western North Pacific.

At longer timescales, our ensemble simulations reveal diverse mean-state changes in the tropical Pacific: CESM2 produces both El Niño–like and La Niña–like SST patterns, while CM2.1 tends to favor La Niña–like conditions. This contrasts with earlier studies that emphasized a robust El Niño–like response to Southern Ocean forcing. Despite these differences, the positive PDO-like SST structure emerges consistently across models and

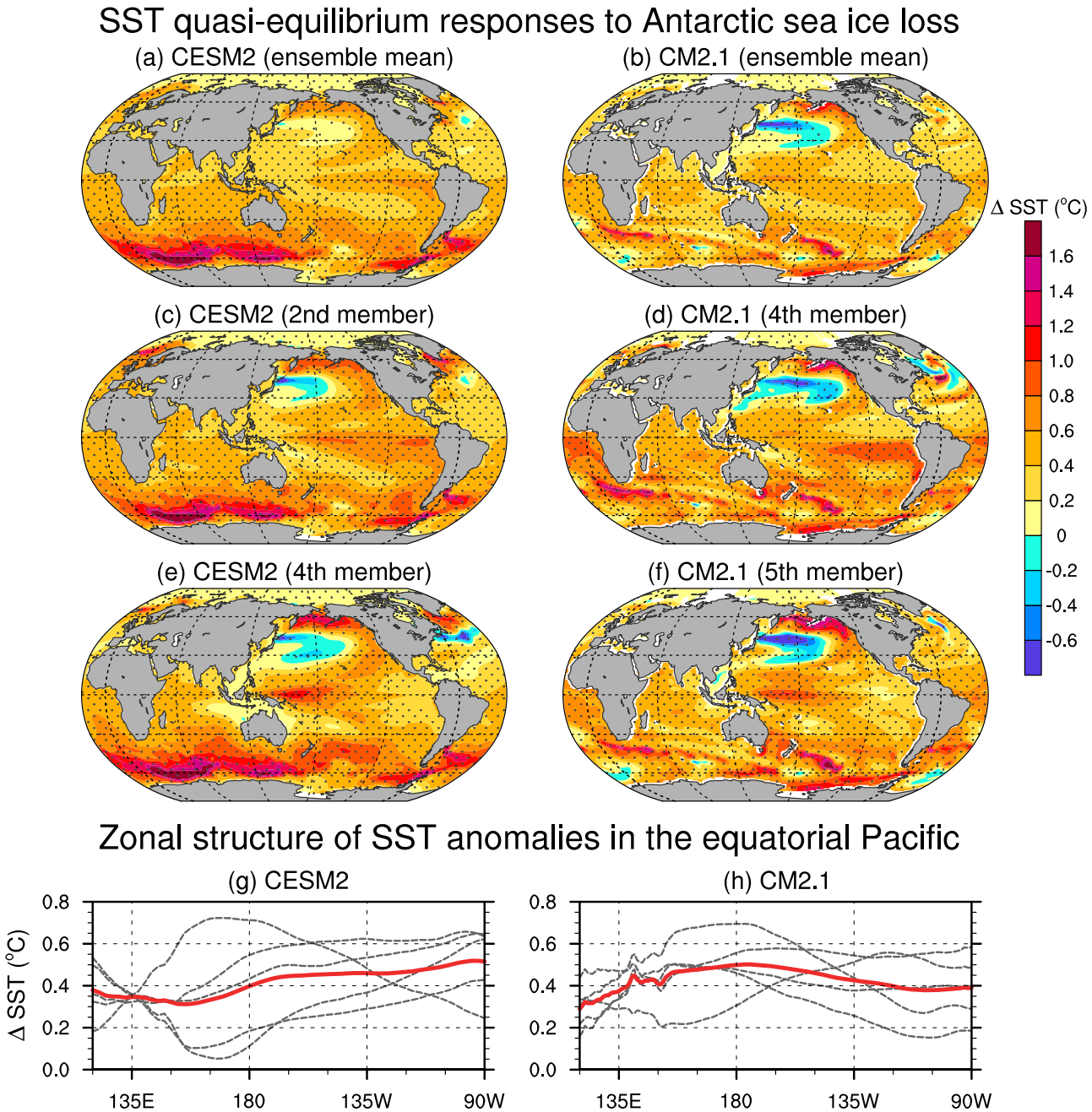


Fig. 5 | Quasi-equilibrium SST responses to Antarctic sea ice loss in CESM2 and CM2.1. a, **b** Ensemble mean, annual-mean SST anomalies (°C, shading) averaged over years 71–100 of the 100-year integration, representing the quasi-equilibrium response, for **a** CESM2 and **b** CM2.1. **c**, **d** Example of individual ensemble members showing an El Niño–like SST warming pattern in CESM2 (2nd member) and CM2.1 (4th member). **e, f** Examples of individual ensemble members showing a La Niña–like SST warming pattern in CESM2 (4th member) and CM2.1 (5th member). **g, h** Zonal structure of SST anomalies (°C) along the equatorial Pacific (15°S–15°N average) for CESM2 and CM2.1. Thin gray dashed lines represent individual ensemble members, and the thick red lines denote the ensemble mean. Stippling indicates statistically significant values ($p < 0.05$).

in most of ensemble members, indicating that extratropical Pacific variability is not solely dependent on tropical Pacific mean states.

Our finding that Antarctic sea-ice loss induces a positive PDO-like pattern complements previous evidence from both observations and models. Ref. 33 linked the late-20th century Antarctic sea-ice expansion to a negative PDO-like state driven by internal tropical variability, while ref. 21 attributed the prolonged negative PDO trend of recent decades to anthropogenic aerosols and greenhouse gases. Recent work by ref. 62 further clarifies the reverse pathway, showing that tropical Pacific variability can drive Antarctic sea-ice changes via poleward-propagating Rossby waves.

Taken together with our results, these studies suggest a bidirectional teleconnection—or more broadly, a coupled feedback system—between the two regions: while past sea-ice expansion coincided with negative PDO-like states, our experiments demonstrate that sea-ice loss can actively reorganize PDO-like variability. The recent record-low Antarctic sea-ice extent in 2023–24 (Supplementary Fig. 6) underscores the near-term relevance of this linkage, indicating that sustained Antarctic sea-ice loss could increase the likelihood of a shift toward a positive PDO in the coming decades, although the exact timing is likely to be strongly modulated by internal variability.

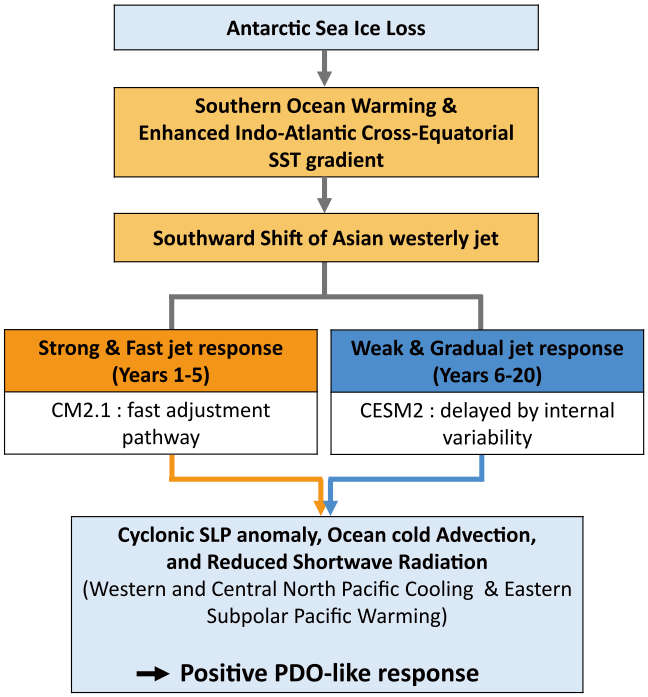


Fig. 6 | Schematic illustration of the dynamical pathway connecting Antarctic sea-ice loss to the development of positive PDO.

By jointly analyzing transient adjustments and quasi-equilibrium responses across two distinct models and multiple ensemble members, our study identifies Antarctic sea-ice loss as a robust driver of cross-hemispheric SST variability. These results emphasize that Antarctic sea-ice decline is not only a high-latitude phenomenon but also a critical factor shaping Pacific decadal variability and, by extension, near-term climate trajectories. It is essential to incorporate Antarctic sea-ice in our conceptual framework to understand and predict global climate evolution.

Methods

Climate models

CESM2. The Community Earth System Model version 2 (CESM2) is used to isolate the remote SST responses to the Antarctic sea ice loss. CESM2 couples with the atmosphere (CAM6; ref. 22), ocean (POP2; ref. 63), and sea ice (CICE5; ref. 64) component models. The horizontal resolution of CAM6 is 2.5° in longitude and 1.9° in latitude. POP2 and CICE5 share a nominal 1° horizontal resolution, with a uniform 1.125° resolution in the zonal direction. The meridional resolution varies, reaching the finest resolution of 0.27° at the equator. In this study, we used the "B1850" compset, in which each component model is active. The B1850 compset is intended as an equilibrium control experiment with constant pre-industrial external forcing.

CM2.1

In addition to CESM2, we also employed the Geophysical Fluid Dynamics Laboratory (GFDL) Climate Model version 2.1 (CM2.1; ref. 23) to investigate the climate response to Antarctic sea ice loss. CM2.1 includes fully coupled components of the atmosphere, land, ocean, and sea ice. The atmosphere and land components have a horizontal resolution of 2.5° longitude × 2° latitude with 24 vertical atmospheric levels. The ocean and sea ice components use a tripolar grid with a nominal horizontal resolution of ~1° and 50 vertical ocean levels.

Experimental design for Antarctic sea ice loss

Control experiment (Ctrl). We conducted control simulations of both CESM2 and CM2.1, each consisting of five ensemble members integrated for 100 years without any changes in sea ice albedo. For CESM2, the initial conditions were derived from restart files provided by NCAR after several hundred years of pre-industrial simulation. For CM2.1, the initial conditions were taken from restart files provided by GFDL following long pre-industrial runs. Ensemble members were generated by applying small perturbations to the atmospheric initial conditions.

To ensure the reliability of the models in capturing North Pacific decadal variability, we evaluated the simulated PDO characteristics in control experiments. Both CESM2 and CM2.1 successfully reproduce the key spatial features of the observed PDO, demonstrating high pattern correlation coefficients (PCCs) exceeding 0.80 with observations (PCC = 0.82 for CESM2 and 0.86 for CM2.1; Supplementary Fig. 11). They clearly capture the characteristic PDO pattern, featuring cooling in the central and western North Pacific and the opposite sign (warming) in the eastern and subpolar Pacific, which resembles a horseshoe shape. Furthermore, spectral analysis confirms that both models capture the realistic spectral peaks on decadal to interdecadal timescales, consistent with observations (e.g., ERSSTv5). These validations demonstrate that the control simulations provide a realistic baseline for investigating the response of North Pacific variability to external forcing.

Reduced Antarctic sea ice albedo experiment (rALB). We conducted idealized experiments with reduced Antarctic sea ice albedo to isolate the climate responses to Antarctic sea ice loss. In CESM2, five ensemble members were integrated for 100 years with a ~25% reduction in Antarctic sea ice albedo, while no changes were applied to the Arctic Ocean, ensuring that only Antarctic sea ice was affected. In CM2.1, five ensemble members were also integrated for 100 years, but with a stronger reduction: members 1–3 used a 40% reduction, and members 4–5 used a 60% reduction. These larger reductions were necessary to account for the substantially weaker sea ice–albedo feedback in CM2.1 (ref. 26).

Previous studies[65,66] demonstrated the usefulness of an albedo-reduction strategy, in which sea-ice albedo was artificially decreased in both hemispheres to investigate the global climate impacts of polar sea-ice loss. This approach has the advantage of modifying sea ice interactively without directly imposing SST or surface heat flux anomalies, thereby preserving energy balance. Building on this framework, our rALB experiments reduce sea-ice albedo only in the Antarctic, enabling us to isolate the distinct role of Antarctic sea-ice decline in shaping the climate response.

As in the control simulations, ensemble members were generated by perturbing the atmospheric initial conditions.

To assess the climate impact of Antarctic sea ice loss, we subtracted the control simulations from the reduced Antarctic sea ice albedo experiments (rALB minus Ctrl). Further details of the Ctrl and rALB experiments, including ensemble configuration and experimental design, are summarized in Supplementary Table 1.

Experimental design for the Asian jet southward shift

To assess the role of the southward shift of the Asian jet over the Tibetan Plateau in shaping the delayed ocean warming in the northwestern Pacific, we conducted an additional idealized experiment using zonal wind (U) nudging. In these experiments, the model's zonal wind over the Tibetan Plateau (28°–53°N, 40°–90°E; the green box in Fig. 4a) was nudged toward a prescribed monthly climatological zonal wind profile according to the following equation:

$$F_{nudge} = \frac{\alpha}{\Delta t_{nudge}}\left(U_{target}(t_{next}) - U_{model}(t_{current})\right) \quad (1)$$

where F_{nudge} is the nudging term that corrects the model's zonal wind toward the target field, U_{target} is the monthly climatological zonal wind from the reference experiment and U_{model} is the simulated state. The nudging is updated every 24 h (t_{next}), while the correction is applied at each model time step ($\Delta t = 1800$ s). The normalized nudging strength coefficient (α) is set to

1 throughout the nudging domain, with a relaxation timescale of $\Delta t_{nudge} =$ 12 h (0.5 days).

Two separate sets of nudging experiments were performed using CESM2. In the first, the zonal wind was nudged toward the 1–30 year monthly climatology from the Ctrl simulation; in the second, the target was the 1–30 year monthly climatology from the rALB simulation. Each nudging experiment consisted of three ensemble members, integrated for 30 years each. The difference between these two nudging experiments (rALB-nudge minus Ctrl-nudge) isolates the climate response associated with the southward shift of the Asian jet. The horizontal distribution of the 200-hPa zonal wind (U200) over the Tibetan Plateau that defines the nudging region is shown in Fig. 4a, and its latitude–pressure (Lev–Lat) cross-section is presented in Fig. 4b. Further details of the Asian jet nudging experiments, including ensemble configuration and experimental design, are summarized in Supplementary Table 2.

Mixed-layer heat budget and term diagnostics

We diagnose the mixed-layer heat budget in flux units (W m^{-2}) and retain the two dominant contributors for summer midlatitudes—diabatic surface heating (with a penetrative shortwave correction) and horizontal temperature advection. Let T_m denote the mixed-layer temperature (SST), h the mixed-layer depth (MLD), ρ_0 seawater density, and C_p heat capacity.

$$\rho_0 C_p h \frac{\partial T_m}{\partial t} \approx Q_{diab} + Q_{adv}, \tag{2}$$

Diabatic surface heating: The effective diabatic forcing of the mixed layer is the net surface heat flux minus the penetrative shortwave that warms waters below the MLD:

$$Q_{diab} = \left(Q_{net} - Q_{pen}\right) = Q_{SW} - Q_{pen} + Q_{LW} + Q_{LH} + Q_{SH}, \tag{3}$$

where Q_{SW} is the downward shortwave at the ocean surface, Q_{LW} net longwave radiation, Q_{LH} latent and Q_{SH} sensible heat flux (all positive downward). The term $(Q_{SW} - Q_{pen})$ represents the effective shortwave heating of the mixed layer. The penetrative shortwave component is estimated following the CESM2 ocean model (POP2) implementation of Jerlov water types, which applies a two-band Beer's law parameterization:

$$Q_{pen} = Q_{SW}\left[r_f e^{-\frac{h}{d_1}} + \left(1 - r_f\right) e^{-\frac{h}{d_2}}\right], \tag{4}$$

where r_f is the fraction of the first band and d_1, d_2 are the attenuation depths. For the default Jerlov type I (clear ocean water) used in CESM2, we adopt $r_f = 0.58, d_1 = 0.35m$, and $d_2 = 23.0m$. We confirmed that Q_{pen} is small compared to the other surface flux terms and therefore neglected it in our subsequent analyses.

Horizontal temperature advection: Mixed-layer horizontal advection is

$$Q_{adv} = -\rho_0 C_p h(\boldsymbol{U}_m \cdot \nabla_h T_m), \tag{5}$$

where $\boldsymbol{U}_m$ are mixed-layer horizontal velocities and ∇_h is horizontal gradients.

For the difference between the rALB and Ctrl experiments, we first diagnose separately from each simulation using Eqs. (3–5). The difference between the two experiments is then obtained as

$$\Delta Q_{adv} = Q_{adv}^{rALB} - Q_{adv}^{Ctrl}, \tag{6}$$

$$\Delta Q_{diab} = Q_{diab}^{rALB} - Q_{diab}^{Ctrl} \tag{7}$$

Data availability

Climate model outputs for CESM2 and CM2.1 simulations conducted for this study are available for download from https://doi.org/10.5061/dryad.z8w9ghxsh.

Code availability

The CESM source code and the standard setup files can be obtained from https://escomp.github.io/CESM/versions/cesm2.1/html/introduction.html. The GFDL CM2.1 model and corresponding data are available from the GFDL portal server (https://data1.gfdl.noaa.gov/CM2.X). The data analysis was conducted using the software CDO and NCL. The analysis codes used for data processing and generating the results presented in this study are also available for download from https://doi.org/10.5061/dryad.z8w9ghxsh.

Received: 30 September 2025; Accepted: 28 March 2026;
Published online: 11 April 2026

References

1. Fogt, R. L., Sleinkofer, A. M., Raphael, M. N. & Handcock, M. S. A regime shift in seasonal total Antarctic sea ice extent in the twentieth century. *Nat. Clim. Change* **12**, 54–62 (2022).
2. Purich, A. & Doddridge, E. W. Record low Antarctic sea ice coverage indicates a new sea ice state. *Commun. Earth Environ.* **4**, 314 (2023).
3. Kuhlbrodt, T., Swaminathan, R., Ceppi, P. & Wilder, T. A glimpse into the future: the 2023 ocean temperature and sea ice extremes in the context of longer-term climate change. *Bull. Am. Meteorol. Soc.* **105**, E474–E485 (2024).
4. Josey, S. A. et al. Record-low Antarctic sea ice in 2023 increased ocean heat loss and storms. *Nature* **636**, 635–639 (2024).
5. Abram, N. J. et al. Emerging evidence of abrupt changes in the Antarctic environment. *Nature* **644**, 621–633 (2025).
6. Cai, W. et al. Southern Ocean warming and its climatic impacts. *Sci. Bull.* **68**, 946–960 (2023).
7. Kang, S. M., Ceppi, P., Yu, Y. & Kang, I.-S. Recent global climate feedback controlled by Southern Ocean cooling. *Nat. Geosci.* **16**, 775–780 (2023).
8. Hay, S. & Kushner, P. J. The relative importance of Antarctic sea ice loss within the response to greenhouse warming. *J. Clim.* **37**, 3323–3344 (2024).
9. Zhang, X. & Deser, C. Tropical and Antarctic sea ice impacts of observed Southern Ocean warming and cooling trends since 1949. *npj Clim. Atmos. Sci.* **7**, 197 (2024).
10. Luo, F., Xie, S. P., Ying, J., Geng, Y. F. & Chen, D. Impacts of Antarctic sea ice change on global warming pattern inferred from CMIP6 intermodel spread. *Geophys. Res. Lett.* **52**, e2024GL112323 (2025).
11. Kim H. et al. Higher precipitation in East Asia and western United States expected with future Southern Ocean warming. *Nat. Geosci.* 2025: 1–9.
12. Jeong, H., Park, H.-S., Kang, S. M. & Chung, E.-S. The greater role of Southern Ocean warming compared to Arctic Ocean warming in shifting future tropical rainfall patterns. *Nat. Commun.* **16**, 2790 (2025).
13. Hudson S. R. Estimating the global radiative impact of the sea ice–albedo feedback in the Arctic. *J. Geophys. Res. Atmos.* **116** (2011).
14. Graversen, R. G. & Wang, M. Polar amplification in a coupled climate model with locked albedo. *Clim. Dyn.* **33**, 629–643 (2009).
15. England, M. R., Polvani, L. M., Sun, L. & Deser, C. Tropical climate responses to projected Arctic and Antarctic sea-ice loss. *Nat. Geosci.* **13**, 275–281 (2020).
16. Wunderling, N., Willeit, M., Donges, J. F. & Winkelmann, R. Global warming due to loss of large ice masses and Arctic summer sea ice. *Nat. Commun.* **11**, 5177 (2020).
17. Duspayev, A., Flanner, M. & Riihelä, A. Earth's sea ice radiative effect from 1980 to 2023. *Geophys. Res. Lett.* **51**, e2024GL109608 (2024).

18. Kim, H., Kang, S. M., Kay, J. E. & Xie, S.-P. Subtropical clouds key to Southern Ocean teleconnections to the tropical Pacific. *Proc. Natl. Acad. Sci.* **119**, e2200514119 (2022).
19. Dong, Y., Armour, K. C., Battisti, D. S. & Blanchard-Wrigglesworth, E. Two-way teleconnections between the Southern Ocean and the tropical Pacific via a dynamic feedback. *J. Clim.* **35**, 6267–6282 (2022).
20. Hwang, Y. T., Xie, S. P., Deser, C. & Kang, S. M. Connecting tropical climate change with Southern Ocean heat uptake. *Geophys. Res. Lett.* **44**, 9449–9457 (2017).
21. Klavans J. M. et al. Human emissions drive recent trends in North Pacific climate variations. *Nature* **644**, 1–9 (2025).
22. Danabasoglu, G. et al. The Community Earth System Model version 2 (CESM2). *J. Adv. Model Earth Syst.* **12**, e2019MS001916 (2020).
23. Delworth, T. L. et al. GFDL's CM2 global coupled climate models. Part I: formulation and simulation characteristics. *J. Clim.* **19**, 643–674 (2006).
24. Sadai, S., Condron, A., DeConto, R. & Pollard, D. Future climate response to Antarctic Ice Sheet melt caused by anthropogenic warming. *Sci. Adv.* **6**, eaaz1169 (2020).
25. Liu, J. & Zhu, Z. Projected Antarctic sea ice change contributes to increased occurrence of strong El Niño. *npj Clim. Atmos. Sci.* **7**, 233 (2024).
26. Winton, M. Sea ice-albedo feedback and nonlinear Arctic climate change. In: *Arctic Sea Ice Decline: Observations, Projections, Mechanisms, and Implications*. Volume 180 (eds DeWeaver, E.T., Bitz, C. M. Tremblay, L.-B.) 111–131 (AGU, 2008).
27. Watanabe, M. et al. Improved climate simulation by MIROC5: mean states, variability, and climate sensitivity. *J. Clim.* **23**, 6312–6335 (2010).
28. Meehl, G. A., Hu, A., Arblaster, J. M., Fasullo, J. & Trenberth, K. E. Externally forced and internally generated decadal climate variability associated with the Interdecadal Pacific Oscillation. *J. Clim.* **26**, 7298–7310 (2013).
29. Qu X., Huang G. Impacts of tropical Indian Ocean SST on the meridional displacement of East Asian jet in boreal summer. *Int. J. Climatol.* **32** (2012).
30. Hong, X. & Lu, R. The meridional displacement of the summer Asian jet, Silk Road pattern, and tropical SST anomalies. *J. Clim.* **29**, 3753–3766 (2016).
31. Cook, K. H. & Held, I. M. The stationary response to large-scale orography in a general circulation model and a linear model. *J. Atmos. Sci.* **49**, 525–539 (1992).
32. Held, I. M., Ting, M. & Wang, H. Northern winter stationary waves: theory and modeling. *J. Clim.* **15**, 2125–2144 (2002).
33. Chung, E.-S. et al. Antarctic sea-ice expansion and Southern Ocean cooling linked to tropical variability. *Nat. Clim. Change* **12**, 461–468 (2022).
34. Patterson, M. & O'Reilly, C. H. Climate models struggle to simulate observed North Pacific jet trends, even accounting for tropical Pacific sea surface temperature trends. *Geophys. Res. Lett.* **52**, e2024GL113561 (2025).
35. Huang, G. et al. A review about Indian Ocean basin mode and its impacts on East Asian summer climate. *Chin. J. Atmos. Sci.* **40**, 121–130 (2016).
36. Liu, S. & Duan, A. Impacts of the leading modes of tropical Indian Ocean sea surface temperature anomaly on sub-seasonal evolution of the circulation and rainfall over East Asia during boreal spring and summer. *J. Meteorol. Res.* **31**, 171–186 (2017).
37. Patterson, M., O'Reilly, C., Woollings, T., Weisheimer, A. & Wu, B. SST-driven variability of the East Asian summer jet on a decadal time-scale in CMIP6 models. *Q. J. R. Meteorol. Soc.* **148**, 581–598 (2022).
38. Donohoe, A., Marshall, J., Ferreira, D. & Mcgee, D. The relationship between ITCZ location and cross-equatorial atmospheric heat transport: From the seasonal cycle to the Last Glacial Maximum. *J. Clim.* **26**, 3597–3618 (2013).
39. Byrne, M., Pendergrass, A., Rapp, A. & Wodzicki, K. Response of the Intertropical Convergence Zone to Climate Change: Location, Width, and Strength. *Curr. Clim. Change Rep.* **4**, 355–370 (2018).
40. Geen, R., Bordoni, S., Battisti, D. S. & Hui, K. Monsoons, ITCZs, and the concept of the global monsoon. *Rev. Geophys.* **58**, e2020RG000700 (2020).
41. Lin, L. et al. Atlantic origin of the increasing Asian westerly jet interannual variability. *Nat. Commun.* **15**, 2155 (2024).
42. Kang, S. M. Extratropical influence on the tropical rainfall distribution. *Curr. Clim. Change Rep.* **6**, 24–36 (2020).
43. Donohoe, A., Armour, K. C., Roe, G. H., Battisti, D. S. & Hahn, L. The partitioning of meridional heat transport from the last glacial maximum to CO 2 quadrupling in coupled climate models. *J. Clim.* **33**, 4141–4165 (2020).
44. Staten, P. W., Lu, J., Grise, K. M., Davis, S. M. & Birner, T. Re-examining tropical expansion. *Nat. Clim. Chang.* **8**, 768–775 (2018).
45. Grise, K. M. et al. Recent tropical expansion: natural variability or forced response?. *J. Clim.* **32**, 1551–1571 (2019).
46. Shaw, T. et al. Storm track processes and the opposing influences of climate change. *Nat. Geosci.* **9**, 656–664 (2016).
47. Wang, T. et al. Meridional position changes of the sea surface temperature anomalies in the North Pacific. *J. Clim.* **35**, 305–321 (2022).
48. Yang J., Liu Q., Xie S. P., Liu Z., Wu L. Impact of the Indian Ocean SST basin mode on the Asian summer monsoon. *Geophys. Res. Lett.* **34** (2007).
49. Xie, S.-P. et al. Indian Ocean capacitor effect on Indo–western Pacific climate during the summer following El Niño. *J. Clim.* **22**, 730–747 (2009).
50. Henley, B. J. Pacific decadal climate variability: Indices, patterns and tropical-extratropical interactions. *Glob. Planet. Change* **155**, 42–55 (2017).
51. Johnson, Z. F., Chikamoto, Y., Wang, S.-Y. S., McPhaden, M. J. & Mochizuki, T. Pacific decadal oscillation remotely forced by the equatorial Pacific and the Atlantic Oceans. *Clim. Dyn.* **55**, 789–811 (2020).
52. Feng, X. et al. Comprehensive representation of tropical–extratropical teleconnections obstructed by tropical Pacific convection biases in CMIP6. *J. Clim.* **36**, 7041–7059 (2023).
53. Yu, J. Y., Liu, W. T. & Mechoso, C. R. An SST anomaly dipole in the northern subtropical Pacific and its relationships with ENSO. *Geophys. Res. Lett.* **27**, 1931–1934 (2000).
54. Stuecker, M. F. Revisiting the Pacific meridional mode. *Sci. Rep.* **8**, 3216 (2018).
55. Tao, L., Yang, X.-Q., Fang, J. & Sun, X. PDO-related wintertime atmospheric anomalies over the midlatitude North Pacific: Local versus remote SST forcing. *J. Clim.* **33**, 6989–7010 (2020).
56. Vijverberg, S. & Coumou, D. The role of the Pacific Decadal Oscillation and ocean-atmosphere interactions in driving US temperature predictability. *Npj Clim. Atmos. Sci.* **5**, 18 (2022).
57. Ueno, H. et al. Review of oceanic mesoscale processes in the North Pacific: physical and biogeochemical impacts. *Prog. Oceanogr.* **212**, 102955 (2023).
58. Newman, M. et al. The Pacific decadal oscillation, revisited. *J. Clim.* **29**, 4399–4427 (2016).
59. Zhang, Y., Xie, S.-P., Kosaka, Y. & Yang, J.-C. Pacific decadal oscillation: Tropical Pacific forcing versus internal variability. *J. Clim.* **31**, 8265–8279 (2018).
60. Zappa, G. & Shepherd, T. G. Storylines of atmospheric circulation change for European regional climate impact assessment. *J. Clim.* **30**, 6561–6577 (2017).
61. Shepherd, T. G. et al. Storylines: an alternative approach to representing uncertainty in physical aspects of climate change. *Clim. change* **151**, 555–571 (2018).

62. Liu, Y. et al. Decadal oscillation provides skillful multiyear predictions of Antarctic sea ice. *Nat. Commun.* **14**, 8286 (2023).
63. Smith, R. et al. The parallel ocean program (POP) reference manual: ocean component of the community climate system model (CCSM). Rep. LAUR-01853 141, 1–141 (2010).
64. Hunke E. C., Lipscomb W. H., Turner A. K., Jeffery N., Elliott S. CICE: The Los Alamos Sea ice model documentation and software user's manual version 5.1 LA-CC-06-012. 675: 15 (T-3 Fluid Dynamics Group, Los Alamos National Laboratory, 2010).
65. Blackport, R. & Kushner, P. J. Isolating the atmospheric circulation response to Arctic sea ice loss in the coupled climate system. *J. Clim.* **30**, 2163–2185 (2017).
66. Blackport, R. & Kushner, P. J. The role of extratropical ocean warming in the coupled climate response to Arctic sea ice loss. *J. Clim.* **31**, 9193–9206 (2018).

Acknowledgements

This work was supported by the Korea Meteorological Administration Research and Development Program (grant: RS-2025-02313090). H.J. was supported by the National Research Foundation of Korea(NRF) grant funded by the Korea government(MSIT) (No. RS-2026-25468388). E.-S.C. was supported by Korea Polar Research Institute (KOPRI) grant funded by the Ministry of Oceans and Fisheries (KOPRI PE26030). The main calculations were performed by the supercomputing resource of the Korea Meteorological Administration (National Center for Meteorological Supercomputer).

Author contributions

H.-S.P. conceptualized, designed the study, and wrote the initial manuscript draft. H.J. conducted the CESM2 and CM2.1 simulations, performed the analysis under the guidance of H.-S.P., S.-W.Y., E.-S.C. and S.-P.X. All authors contributed to interpreting the results and writing the manuscript.

Competing interests

The authors declare no competing interests.

Additional information

Supplementary information The online version contains supplementary material available at https://doi.org/10.1038/s43247-026-03489-w.

Correspondence and requests for materials should be addressed to Hyo-Seok Park.

Peer review information *Communications Earth and Environment* thanks Cheng Sun and the other, anonymous, reviewer(s) for their contribution to the peer review of this work. Primary Handling Editor: ChenRui Diao. A peer review file is available.

Reprints and permissions information is available at http://www.nature.com/reprints

Publisher's note Springer Nature remains neutral with regard to jurisdictional claims in published maps and institutional affiliations.

Open Access This article is licensed under a Creative Commons Attribution-NonCommercial-NoDerivatives 4.0 International License, which permits any non-commercial use, sharing, distribution and reproduction in any medium or format, as long as you give appropriate credit to the original author(s) and the source, provide a link to the Creative Commons licence, and indicate if you modified the licensed material. You do not have permission under this licence to share adapted material derived from this article or parts of it. The images or other third party material in this article are included in the article's Creative Commons licence, unless indicated otherwise in a credit line to the material. If material is not included in the article's Creative Commons licence and your intended use is not permitted by statutory regulation or exceeds the permitted use, you will need to obtain permission directly from the copyright holder. To view a copy of this licence, visit http://creativecommons.org/licenses/by-nc-nd/4.0/.

© The Author(s) 2026